ACS Catalysis

Research Article

pubs.acs.org/acscatalysis

Confinement Effect of Carbon Nanotubes: Copper Nanoparticles Filled Carbon Nanotubes for Hydrogenation of Methyl Acetate

Ding Wang,[†] Guohui Yang,[†] Qingxiang Ma,[†] Mingbo Wu,*[,‡] Yisheng Tan,[§] Yoshiharu Yoneyama,[†] and Noritatsu Tsubaki*[,†]

[†]Department of Applied Chemistry, Graduate School of Engineering, University of Toyama, Gofuku 3190, Toyama 930-8555, Japan
[‡]State Key Laboratory of Heavy Oil Processing, China University of Petroleum, Shandong, Qingdao 266555, P. R. China
[§]Institute of Coal Chemistry, Chinese Academy of Sciences, Taiyuan 030001, P. R. China

ABSTRACT: Copper nanoparticles filled carbon nanotubes (CNTs) with varied tube diameters were prepared via a convenient sonication-assisted impregnation approach. CNTs and Cu nanoparticles filled CNTs were thoroughly investigated using transmission electron microscopy, Raman spectroscopy, N_2 adsorption, X-ray diffraction, and H_2 temperature programmed reduction. Confinement effects of CNTs, originated from its diameter and microstructure, on the filled Cu nanoparticles were discovered. For CNTs with smaller tube diameter, a consequential strong autoreduction for the confined Cu nanoparticles was observed, which showed a downward trend with the increasing anneal temperature. Methyl acetate (MeOAc) hydrogenation forming methanol and ethanol was chosen as model reaction to further explore the influence of CNTs confinement effects on the catalytic performance. In the case of catalysts derived from CNTs with smaller inner diameter (4−10 nm), their catalytic performance were improved after the CNTs heat treatment under Ar atmosphere and the optimum treatment temperature was 973 K. On the contrary, the CNTs catalysts with larger inner diameter (20−30 nm) exhibited reduced catalytic activity after the same heat treatment. In addition, the selectivity to ethanol from MeOAc was also found dependent on CNTs tube diameter. Furthermore, the Cu nanoparticles loaded outside of CNTs catalyst were prepared and compared with the Cu nanoparticles filled inside CNTs catalyst, and the latter exhibited higher catalytic activity because of the confinement effects of CNTs. All in all, when using CNTs as support materials, the likely synergistic effects created by CNTs diameter, the pretreatment on CNTs, and the nanocatalyst loaded inside or outside CNTs are responsible for the catalytic activity of the prepared catalysts. These findings propose an in-depth insight into the confinement of CNTs to the filled metal catalysts, and thus inspire the development of novel catalyst with beneficial catalytic performance.

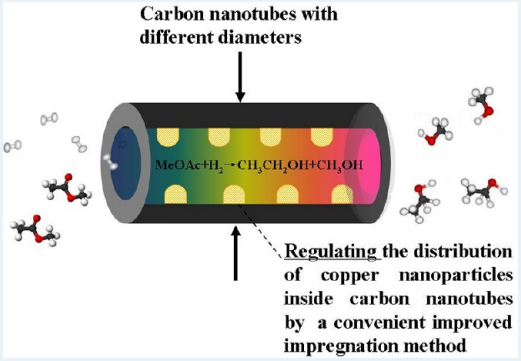

KEYWORDS: *confinement effect, hydrogenation, carbon nanotubes, Cu catalyst, methyl acetate, autoreduction effect*

1. INTRODUCTION

Carbon nanotubes (CNTs), a member of carbon materials with graphite layers and tubular structure, were first discovered by Iijima as a byproduct in fullerene synthesis.[1] CNTs are ideal catalyst supports because of their excellent performance such as high surface area, excellent electronic conductivity, and good resistance to acidic/basic chemicals even at high temperature.[2] To date, many metals, for example, Au, Ag, Pt, Ru, Rh, Pd, Ni, Zn, Co, and Fe decorated CNTs, have been studied as the catalysts for liquid-phase (hydrogenation, hydroformylation) or gas-phase (Fischer−Tropsch synthesis, ammonia synthesis and decomposition) catalytic reactions.[3−6] It is noteworthy that CNTs-based catalysts often show higher activity and/or selectivity than other catalysts with metal nanoparticles supported on conventional supports[7] (such as alumina, silica, or even activated carbon). In particular, the metal nanoparticles filled inside CNTs catalysts usually show higher activity than the loaded outside catalysts for applications in catalysis, which is attributed to the confinement effects of CNTs.[8] Confinement effect within CNTs or porous materials can affect chemical reactions through a host of varied aspects, such as changes in thermodynamic state of the system because of interactions with inside walls, selective gas adsorption, and geometrical constraints that affect the reaction mechanism.[9] The confinement effects of CNTs was investigated usually by loading metal such as Fe, Co, Ni, Au, Ru, and Rh nanoparticles inside or outside CNTs,[10−14] which was usually investigated from the different electronic properties of inner and outer surfaces of CNTs. The other factors, such as the functional groups and defects on the inner surface of wall, were barely taken into account. In addition, the influences of CNTs diameter on outside loaded Co catalyst were studied previously through Fischer−Tropsch reaction, and the outcomes illustrated that the catalytic performance was not influenced by tube

Received: April 9, 2012
Revised: July 28, 2012
Published: August 8, 2012

diameter.[14] However, the effects of CNTs inner diameter to the catalytic performance of confined catalysts were equally important yet seldom reported.

Cu and Cu_xO (CuO, Cu_2O) have attracted extensive attention because of their wide applications in hydrogenation,[15] low temperature methanol synthesis,[16] water gas shift reaction,[17] click chemistry[18−20] and coupling reactions.[21,22] The Cu or Cu_xO nanoparticles loaded on CNTs had been prepared by physical methods such as arc-discharge,[23] chemical vapor deposition,[24] supercritical CO_2 fluid methods,[25] as well as by chemical methods including electrochemical codeposition,[26] ethylene glycol reduction,[27] solution infusion methods,[28] and so forth. Normally, these methods are relatively complicated and thus can not readily control the fixed position of Cu nanoparticles inside CNTs. To our knowledge, the controlled loading of nanoparticles inside CNTs is considerably crucial to the confinement effect of CNTs on catalyst performance.

Herein, we report a simple wet chemical method to fill Cu nanoparticles into CNTs. The CNTs and Cu nanoparticles filled CNTs were systematically analyzed by transmission electron microscopy (TEM), X-ray diffraction (XRD), Raman spectroscopy, N_2 adsorption and H_2 temperature programmed reduction (TPR). Methyl acetate (MeOAc) hydrogenation in gas phase was chosen as probe reaction to explore the catalytic performance of obtained catalysts as well as the effects of CNTs diameter and heat treatment on catalytic performance. The method to design CNTs filling catalyst and perspective to investigate the confinement effects of CNTs may enlighten readers to synthesize and design other related catalyst with beneficial performance.

2. EXPERIMENTAL DETAILS

2.1. Catalyst Preparation. Multiwall CNTs with small diameter (inner diameter: 4−10 nm; length: 0.5−2 μm; Chengdu, China) and large diameter (inner diameter: 20−30 nm; length: 1−10 μm; Chengdu, China) were used as catalyst support. $Cu(NO_3)_2{\cdot}3H_2O$ was purchased from Kanto Chemical Co. and used without further purification.

Prior to impregnation, the raw CNTs were refluxed with 65% HNO_3 at 393 K for 14 h, followed by washing with deionized water until pH = 7, and then dried over 12 h at 333 K. These CNTs were vacuum treated at 353 K for 12 h. The CNTs with smaller inner diameter was defined as S-CNTs and with the larger inner diameter was defined as L-CNTs. S-CNTs or L-CNTs annealed at 673 K, 973 or 1173 K for 3 h with Ar as protective gas were defined as S-673, S-973, S-1173 or L-673, L-973, L-1173, respectively.

The preparation of Cu nanoparticles filled CNTs catalysts was as follows: S-CNTs of 0.5 g was impregnated with 1 mL of $Cu(NO_3)_2$ solution with concentration 0.868 mol/L, sonicated and stirred for 30 min. Another 0.5 mL of deionized water was added dropwise, sonicated for 30 min, and then a dry sample was obtained. Subsequently, the obtained sample was dried slowly to 373 K and kept for 10 h. The final catalyst was obtained by calcining the dried sample at 623 K under Ar atmosphere for 3 h. The Cu nanoparticles filled S-CNTs catalyst was defined as Cu-S. The Cu nanoparticles filled the heat treated CNTs (S-673, S-973, and S-1173) catalysts were prepared by the same process and was noted as Cu-S-673, Cu-S-973, or Cu-S-1173, respectively. The Cu contents of all catalysts were 10.0 wt %.

The L-CNTs treated by the same process yet filled with 10.0 wt % Cu nanoparticles were defined as Cu-L, Cu-L-673, Cu-L-973, or Cu-L-1173, respectively.

Cu loaded outside CNTs was obtained from incipient wetness impregnation method with the ends closed CNTs as support. The CNTs with the ends closed (C-S-CNTs) were prepared by refluxing the raw S-CNTs in dilute nitric acid (37.5%) as described in a previous report.[13] And then, the C-S-CNTs were impregnated with $Cu(NO_3)_2{\cdot}3H_2O$ solution with the ultrasonic assistance, followed by drying at 373 K in Air for 10 h, and calcining at 623 K under Ar for 3 h. The obtained sample was defined as Cu-C-S.

2.2. Characterizations of Catalysts. The morphologies of the samples characterized by high resolution TEM were obtained with a JEOL JEM-2100 UHR transmission electron microscope operated at 200 kV. Raman spectroscopy was recorded using an Ar^+ ion laser at 514.5 nm wavelength (Renishaw inVia 2000 Raman microscope, Renishaw plc, U.K.) to assess the graphitic structure of CNTs. The crystal structure of the materials was confirmed by XRD with a Rigaku D/max-2550 V diffractometer employing Cu Kα radiation (λ = 1.54056 Å; scanning rate: 0.02°/s in the range of 10−70°). The Brunauer−Emmett−Teller (BET) surface area was determined by N_2 adsorption method using an automatic gas adsorption system (Quantachrome, Autosorb-1, Yuasa Co.). The Cu surface area was measured by pulse titration of Cu surface atoms in the prereduced samples with N_2O.[29] The reducibility of catalysts was examined using the H_2 TPR method with BELCAT (BEL Japan Co. Ltd.).

2.3. Catalytic Reaction. All the catalytic reactions were conducted with a fixed-bed stainless steel reactor (9.5 mm OD), and 0.5 g catalyst was loaded into the reactor. Prior to the reaction, the catalysts were reduced in situ by a flow of pure hydrogen at 573 K for 10 h. After cooling to 493 K, the flow rate of pure hydrogen was fixed at 80 mL/min and the reaction pressure 3 MPa. Then, the MeOAc was pumped in at 0.9 g/h. The liquid MeOAc was first evaporated to MeOAc gas by heater band, and then carried into the reactor by the hydrogen flow. Ar, CO, CH_4, CO_2 were analyzed online by a gas chromatograph equipped with thermal conductivity detector (TCD). The liquid products of catalytic reaction were collected with an ice−water trap using 1-butanol as solvent, and analyzed by another gas chromatograph with flame-ionization detector (FID), in which 1-propanol was employed as the internal standard.

3. RESULTS AND DISCUSSION

3.1. Characterization of Catalyst Supports. Figure 1 shows the morphology of the pristine CNTs and the CNTs after acid treatment. It can be seen that the raw S-CNTs (Figure 1a) was curved and tangled with inner diameter of 4−10 nm and length of 0.5−2 μm. Furthermore, it is also clear that the raw S-CNTs contained some metallic particles or amorphous carbon, with their caps mainly closed. In the case of the TEM images of CNTs after acid treatment (Figure 1b and Figure 1c), it is obvious that amorphous carbon and metallic particles were eliminated and most of CNTs's caps were opened, with few damage on the CNTs walls. The morphology of L-CNTs is shown in Figure 1d. The channel diameter of L-CNTs was 20−30 nm.

Raman spectroscopy is a widely used tool for characterization of changes in CNTs structure.[30,31] The Raman spectra of CNTs samples excited with 514.5 nm laser line is given in Figure 2.

dx.doi.org/10.1021/cs300234e | ACS Catal. 2012, 2, 1958−1966

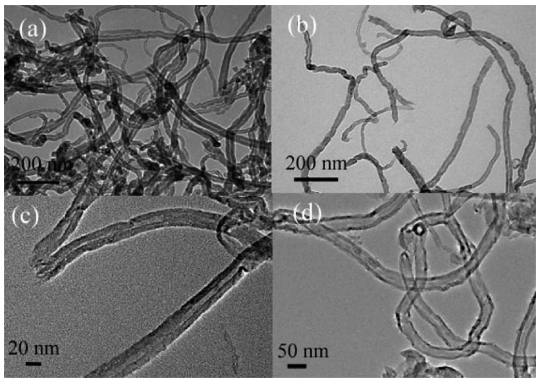

Figure 1. TEM images of CNTs: (a) raw S-CNTs, (b) S-CNTs with low magnification, (c) S-CNTs with high magnification, (d) L-CNTs.

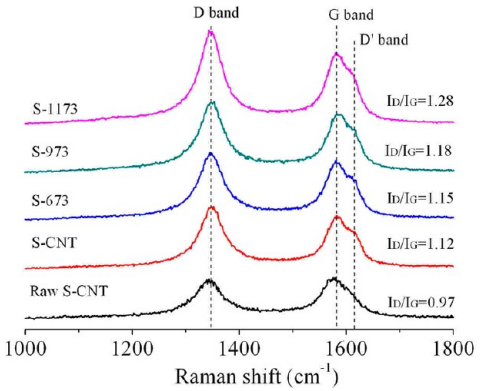

Figure 2. Raman spectra of raw S-CNTs, S-CNTs, S-673, S-973, and S-1173.

The spectra show two major strong peaks at ~1350 cm^{-1} and 1580 cm^{-1}, that is, D and G bands, respectively. The band at ~1610 cm^{-1}, termed D′ band, appears as a high wavenumber shoulder on the G band. The D band is associated with the disorderly structure of graphite, which may be attributed to the defects in curved graphene sheets, tube ends and finite size crystalline domains of the tubes together with the contribution of impurities as amorphous carbon in CNTs. In contrast, the G band corresponds to the structure of the sp^2 hybridized carbon atom, whereas the D′ band is attributed to irregular d_{002} spacing as reported previously.[32−34] Changes in CNTs by acid treatment can be clearly observed by the intensity ratio between the D band and the G band (I_D/I_G). For instance, the I_D/I_G ratio of S-CNTs was enhanced almost 10% compared with that of the raw S-CNTs. The changes of the I_D/I_G ratio in the acid treated CNTs could be due to the introduction of new defects as well as changes in the CNTs geometry caused by the binding of new functional groups or an electrophilic addition at hexatomic-hexatomic boundaries.[35,36] Furthermore, it is found that the G band up-shifted by 10 cm^{-1}, indicating the oxidation process via acid treatment imposed a significant impact on the graphitic wall structure of CNTs. Moreover, the new D′ band peak implies the edge-plane structural disorder during the treatment. Such phenomenon reveals that the surface structure of multiwalled CNTs has been partially damaged, which is consistent with above TEM results. The I_D/I_G ratios of S-CNTs, S-673, S-973, and S-1173 are 1.12, 1.15, 1.18 and 1.28, respectively. The increase in I_D/I_G with increasing anneal temperature was ascribed to the defect or cavity sites formed onto the graphite walls.[37] It is found that the ratios of the I_D/I_G gradually increased before 973 K, and then rapidly increased. The result implies that the graphitic structure of S-CNTs was relatively stable before 973 K. As the anneal temperature went up, the I_D/I_G ratio increased from 1.18 (at 973 K) to 1.28 (at 1173 K), indicating that the functional groups decompose and create new defects on the CNTs surface during 1173 K heat treatment.

To investigate the changes of the specific surface area and porous structure, N_2 adsorption−desorption isotherms and pore size distribution of CNTs before and after acid and heat treatments were measured, and the results are presented in Figure 3. The N_2 adsorption−desorption isotherms of all CNTs samples, given in Figure 3a, belonged to type IV adsorption isotherms with clear hysteresis loops at high relative pressures, indicating the presence of mesopores. The raw S-CNTs showed a low and gradual N_2 uptake at the medium relative pressure (P/P_0) yet a dramatically predominant adsorption at higher P/P_0, which is usually associated with multilayer adsorption on external surfaces and in larger mesopore or macropore formed at spaces between CNTs.[38,39] The N_2 adsorption amount near P/P_0 = 1 decreased clearly after acid treatment, suggesting the big decrease of large mesopore and macropore due to aggregated pores between the CNTs. The hysteresis loop at the medium relative pressure range (P/P_0 = 0.4−0.8) was associated with capillary condensation in small mesopores (3−4 nm), which was consistent with the pore size distribution in Figure 3b. As seen in Figure 3b, there are two types of pores,

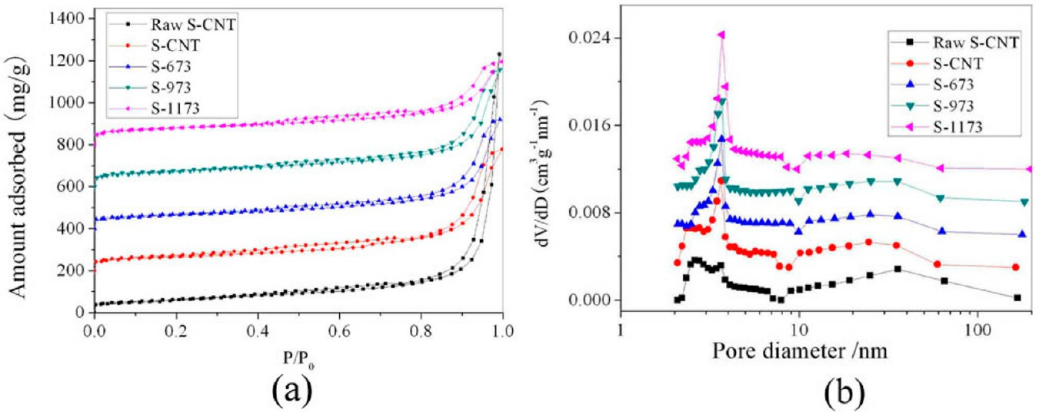

Figure 3. (a) Nitrogen adsorption isotherms and (b) pore size distribution of raw S-CNTs, S-CNTs, S-673, S-973, and S-1173.

dx.doi.org/10.1021/cs300234e | ACS Catal. 2012, 2, 1958−1966

which were assigned as inner pore and aggregated pore.[40] After acid treatment, the peak at 3−5 nm clearly increased, indicating that the ends of CNTs were opened. The specific surface area (as shown in Table 1) increased from 173 m^2/g to 224 m^2/g

Table 1. BET Surface Area and Porosity of S-CNTs Supports

catalyst supports	BET surface area[a] [m^2/g]	V_{Total}[b] [cm^3/g]	V_{micro}[c] [cm^3/g]	V_{meso}[d] [cm^3/g]
Raw S-CNTs	173	1.557	0.072	1.485
S-CNTs	224	0.894	0.100	0.794
S-CNT-673	237	0.884	0.106	0.778
S-CNT-973	251	0.863	0.109	0.754
S-CNT-1173	265	0.612	0.121	0.491

[a]The surface area was determined by N_2 adsorption. [b]V_{Total}: Total pore volume was estimated at a relative pressure $P/P_0 = 0.99$. [c]V_{Micro}: Micropore volume was determined from the Dubinine−Radushkevic (DR) equation. [d]V_{Meso}: Mesopore volume was determined from the subtraction of micropore volume from total pore volume.

after nitric acid treatment, which also illustrated that oxidation of CNTs with nitric acid opened the caps of the CNTs and exposed their internal surface area. The increased micropore volume and decreased mesopore volume after acid treatment suggested the formation of some defects on CNTs walls. The values of micropore volume and mesopore volume experienced regular change when the heat treatment temperature below 973 K. However, the micropore volume increased and mesopore volume decreased notably when the temperature increased from 973 K to 1173 K. These findings indicated that more defects on CNTs were formed at 1173 K, as also supported by the results of Raman spectroscopy.

3.2. Cu Nanoparticles Filled CNTs with Small Inner Diameter. Figure 4 shows the TEM images of Cu-S, Cu-S-673, Cu-S-973, and Cu-S-1173. All samples displayed similar structures with majority of nanoparticles filled inside the channel of CNTs. On the basis of the results of Raman spectroscopy and the pore size distribution, most of the CNTs ends were opened after 65% HNO_3 treatment. Because of the relatively low surface tension of the water and the assistance of sonication, liquid was sucked into the channels of CNTs, driven by the capillary force. Importantly, the water added at the second step helped rinsing the outside residual copper salt into CNTs. The TEM images also displayed that the average size of Cu nanoparticles was about 7.0 nm on Cu-S, 7.8 nm on Cu-S-673, 8.0 nm on Cu-S-973, and 9.7 nm on Cu-S-1173. Detailed size distribution is presented in Figure 4e and Table 2. The increase of Cu nanoparticle size with increasing heat treatment temperature is attributed to the change of CNTs supports.[41−43] It is conceivable that the oxygen-containing functional groups, such as carboxyl group and hydroxyl group, formed both inside and outside CNTs when the caps of CNTs were opened by acid treatment. The Cu^{2+} ions in the solution were preferentially adsorbed onto these functional groups because of electrostatic force when the $Cu(NO_3)_2$ solution was sucked into CNTs. These functional groups could be removed by heat treatment, which therefore led to the nanoparticles inside of CNTs aggregated and grown up.

3.3. Reduction Behavior of Cu Nanoparticles Filled CNTs with Small Inner Diameter. The XRD patterns of Cu-S, Cu-S-673, Cu-S-973, and Cu-S-1173 before reduction are displayed in Figure 5. The peaks at 26.2° observed in all profiles could be indexed as (002) diffractions of graphite (JCPDS 75-

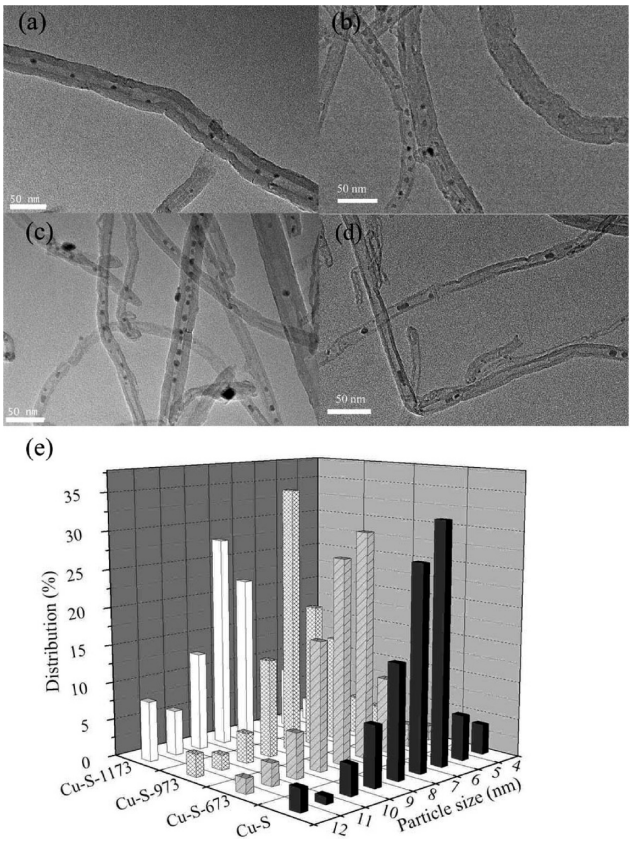

Figure 4. TEM images of (a) Cu-S, (b) Cu-S-673, (c) Cu-S-973, (d) Cu-S-1173, (e) Cu particle size distribution.

Table 2. Physicochemical Properties of the S-CNTs Based Catalysts

catalysts	BET surface area[a] [m^2/g]	total pore volume[a] [cm^3/g]	exposed Cu surface area[b] [m^2/g]	average particle size[c] [nm]
Cu-S	197	0.62	2.8	7.0
Cu-S-673	201	0.75	3.7	7.8
Cu-S-973	224	0.77	4.7	8.0
Cu-S-1173	244	0.70	3.5	9.7

[a]The BET surface area and pore volume were determined by N_2 adsorption. [b]N_2O pulse titration was employed to measure the exposed metallic Cu surface area. [c]The average size of nanoparticles was evaluated from counting and averaging TEM images.

1621). By comparing the intensities of peaks, the Cu-S-1173 with the lowest intensity implies that the damage to it was the biggest. The defects of CNTs can also be observed from TEM images, Raman spectroscopy, and N_2 adsorption. The XRD patterns show that the Cu phase changed from metallic Cu on Cu-S to Cu+Cu_2O on Cu-S-673, to Cu_2O+CuO on Cu-S-973, and finally to CuO on Cu-S-1173, which clarified that the reducibility of CNTs decreased with the increase of heat treatment temperature. A similar autoreduction effect was also reported for Fe, Co, Ni filled CNTs.[44−47] It was proposed that electron deficiency of the CNTs' interior surface is responsible for this phenomenon. In this paper, we found the autoreduction effect also correlated with the functional groups on CNTs introduced by the acid treatment. The crystal phase of Cu

dx.doi.org/10.1021/cs300234e | ACS Catal. 2012, 2, 1958−1966

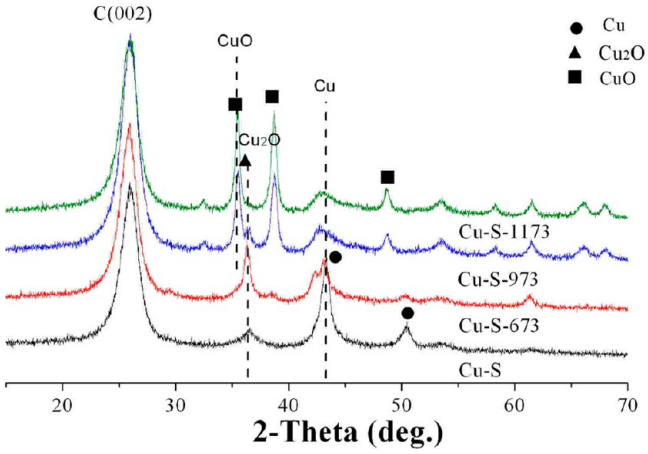

Figure 5. XRD patterns of Cu-S, Cu-S-673, Cu-S-973, and Cu-S-1173.

inside CNTs changed from metallic Cu to CuO with the functional groups removed by heat treatment in Ar atmosphere. The influence of functional groups on autoreduction effect might be achieved through changing the electronic properties of inner surface of CNTs.

The reduction properties of the Cu-S, Cu-S-673, Cu-S-973, and Cu-S-1173 were determined by H_2 temperature programmed reduction (TPR). As shown in Figure 6, all the

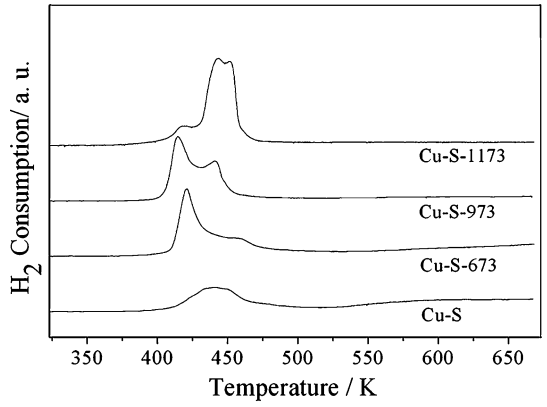

Figure 6. TPR patterns of Cu-S, Cu-S-673, Cu-S-973, and Cu-S-1173.

catalysts showed peaks in beneficial lower temperature ranges than that of pure CuO (513 K) or Cu on Al_2O_3 (503−528 K) or MCM-41 (503−533 K) supports,[48] indicating that CNTs as support enhanced the reducibility of Cu species at low temperature, which may be due to the smaller Cu_xO particle size confined inside CNTs. In Figure 6, the position, width, and intensity of the peaks depended on the pretreatments of S-CNTs. It is noted that only a single and broad peak was observed in Cu-S. Combined with the XRD results, the majority of Cu^{2+} was reduced by CNTs (most probably by its functional groups) after calcination at 623 K under Ar atmosphere. Cu-S-673 and Cu-S-973, as shown in Figure 6, exhibited two peaks. Clearly, the reduction temperature of the first peak was lowered and the hydrogen consumption was increased after heat treatment on S-CNTs. As reported,[49,50] the low-temperature reduction peak and high-temperature reduction peak were attributed to the reduction of highly dispersed Cu_xO and that of bulk Cu_xO, respectively. The fact that reduction peak temperature decreased with the enhanced CNTs' pretreatment temperature might be due to the weak interaction between Cu nanoparticles and CNTs. The decreased reduction temperature is beneficial to increasing the Cu exposed area, which improves the catalyst activity. As shown in Table 2, the reducibility sequence of Cu-S, Cu-S-673, Cu-S-973, and Cu-S-1173 was consistent with the levels of Cu exposed area. However, the reduction temperature of Cu-S-1173 was higher than that of Cu-S-973, inconsistent with the above trend. This different behavior likely comes from the following reasons: The average Cu particle size increased from 8.0 nm of Cu-S-973 to 9.7 nm of Cu-S-1173 as shown in Table 2, which caused the Cu_xO to be reduced with more difficulty.[51,52] Furthermore, as shown in Figure 4, the size of Cu nanoparticles was so large that some nanoparticles blocked the mouths of CNTs. The diffusion of reduction gas could be hindered by the blocked Cu_xO nanoparticle near the mouths of CNTs, which resulted in lower reducibility and higher reduction temperature.

3.4. Cu Nanoparticles Filled Large Inner Diameter CNTs. To investigate the effect of CNTs tube diameter on the catalytic performance, Cu-L catalysts were prepared from larger tube diameter CNTs (inner diameter: 20−30 nm) via the same process. Figure 7 exhibited the TEM images for Cu-L, Cu-L-673, Cu-L-973, and Cu-L-1173 catalysts after 10 h reduction at 573 K with 100% H_2 followed by 3 h passivation with 1% O_2. For these catalysts, nearly all nanoparticles exist inside L-CNTs. As given in Table 3, the average size of Cu nanoparticles was about 15.1 nm on Cu-L, larger than 7.0 nm of Cu nanoparticles on Cu-S. Cu particle size increased with the heat treatment temperature, which was consistent with the change in S-CNTs based catalysts. It is noted that the wall width of L-CNTs decreased and the ratios of wall thickness to inner diameter were about 0.84 for Cu-L, 0.55 for Cu-L-673, 0.57 for Cu-L-973, and 0.44 for Cu-L-1173, which indicated the heat treatment temperature had a significant influence on the wall structure of L-CNTs.

The XRD patterns of Cu-L, Cu-L-673, Cu-L-973, and Cu-L-1173 were given in Figure 8. The intensity of the graphite peak (002) initially decreased and then remained stable from Cu-L to Cu-L-1173 K. This trend was consistent with the change of the ratios of wall thickness to inner diameter as observed by TEM in Figure 7. Peaks of Cu and Cu_2O with similar intensity were observed in the XRD pattern of Cu-L, suggesting that the autoreduction property of L-CNTs was weaker than that of S-CNTs. This phenomenon can be attributed to the varied electronic properties of CNTs' inner surface with different diameters. It is believed that CNTs with smaller tube diameter exhibit stronger autoreduction effect on the metallic nanaoparticles confined inside CNTs. Furthermore, the decrease of autoreduction effect with increasing anneal temperature was also observed here.

The TPR patterns of Cu nanoparticles filled inside L-CNTs and heat treated L-CNTs are exhibited in Figure 9. According to the above analysis, the low-temperature reduction peak (425 K) and high-temperature reduction peak (453 K) are from the reduction of highly dispersed Cu_xO and that of bulk Cu_xO, respectively.[53] The position of the low-temperature peak gradually shifts to lower temperature with increasing pretreatment temperature, which is consistent with the changes of S-CNTs based catalysts. However, it should be noted that the intensity of the low-temperature peak remarkably decreased with increasing pretreatment temperature, which reflects the decreased ratio of highly dispersed Cu_xO in CNTs. In

dx.doi.org/10.1021/cs300234e | ACS Catal. 2012, 2, 1958−1966

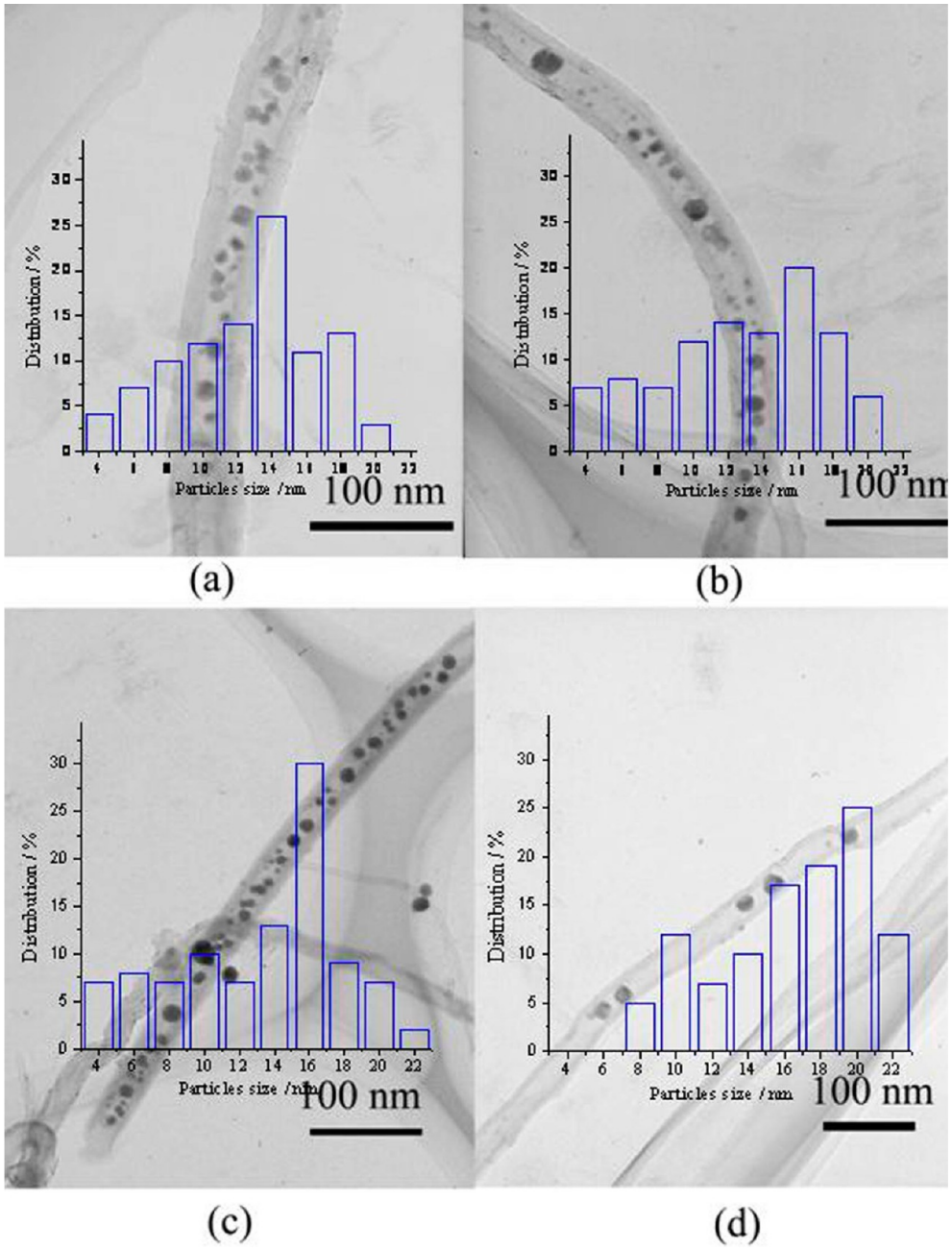

Figure 7. TEM images and Cu size distribution of catalysts after reduction. (a) Cu-L, (b) Cu-L-673, (c) Cu-L-973, (d) Cu-L-1173.

particular, as an evidence of the decreased dispersion with increasing pretreatment temperature, the high-temperature TPR peak shifted to higher temperature accompanied by increasing intensity. The increased ratio of bulk CuO in CNTs was also proved by the TEM image and particle size distribution.

3.5. Methyl Acetate (MeOAc) Hydrogenation on Cu Nanoparticles Filled CNTs Catalysts. MeOAc as byproduct of many industrial productions including polyvinyl alcohol (PVA), acetic acid, is readily available at very low costs, yet has barely been developed toward any economically and technically rewarding applications. Recently, a novel synthesis method to ethanol was reported by dimethyl ether carbonylation and the subsequent hydrogenation of the obtained MeOAc in a dual-catalyst bed reactor.[29,54] MeOAc hydrogenation is a key step in the novel ethanol synthesis route and thus the design and application of hydrogenation catalyst, especially suitable to MeOAc hydrogenation reaction, should be given more attention. In this paper, MeOAc hydrogenation was selected as probe reaction not only to investigate the confinement effects of CNTs to the filled Cu nanoparticles, but also to explore a new catalyst system for MeOAc hydrogenation. Ethyl acetate (EtOAc) was from the secondary reaction of the obtained ethanol via its trans-esterification with MeOAc.

The catalytic performances of S-CNTs based catalysts used for MeOAc hydrogenation are listed in Table 4. Clearly, the catalyst supported on heat treated CNTs had a better catalytic activity than that on S-CNTs. The highest activity was obtained when the S-CNTs annealed at 973 K, exhibiting the conversion of 22.5% and the molar selectivity to ethanol of 27.6%. For Cu-S-1173, MeOAc conversion was lower than that of Cu-S-973, which may be attributed to its increased Cu particle size. In

dx.doi.org/10.1021/cs300234e | *ACS Catal.* 2012, 2, 1958−1966

Table 3. Physicochemical Properties of the L-CNTs Based Catalysts

catalysts	BET surface area[a] [m²/g]	total pore volume[a] [cm³/g]	exposed Cu surface area[b] [m²/g]	average particle size[c] [nm]
Cu-L	139	0.59	3.1	15.1
Cu-L-673	149	0.74	1.7	17.4
Cu-L-973	151	0.72	1.6	18.5
Cu-L-1173	149	0.71	1.6	19.0

[a]The BET surface area and pore volume were determined by N_2 adsorption. [b]N_2O pulse titration was employed to measure the exposed metallic Cu surface area. [c]The average size of nanoparticles was evaluated from counting and averaging TEM images.

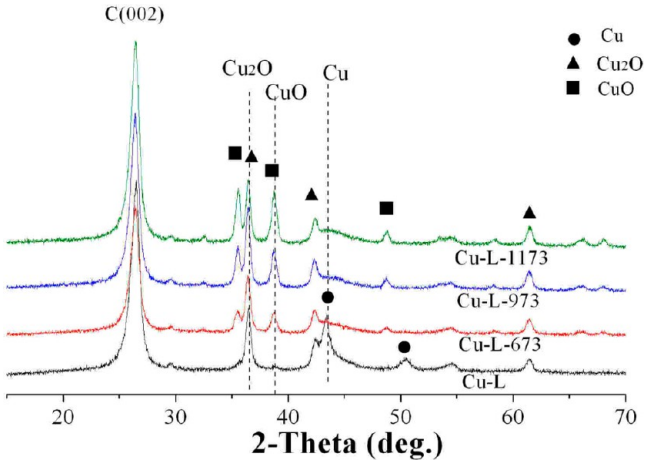

Figure 8. XRD patterns of Cu-L, Cu-L-673, Cu-L-973, and Cu-L-1173.

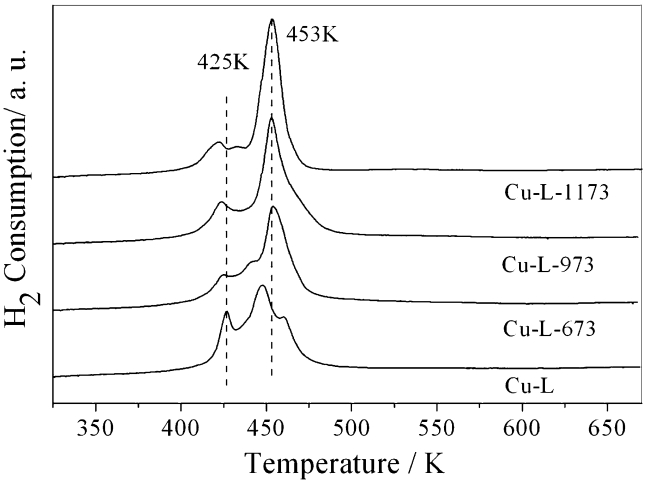

Figure 9. TPR patterns of Cu-L, Cu-L-673, Cu-L-973, and Cu-L-1173.

addition, H_2 TPR also proved the starting reduction temperature of Cu-S-973 lower than that of Cu-S-1173. Table 4 also shows that the turnover frequency (TOF) value increased with the increasing heat treatment temperature and a correlation existed between TOF and Cu crystallite size for this reaction, which appears to be structure-sensitive.

In contrast with the above S-CNTs based catalysts, L-CNTs catalysts annealed at high temperature had a lower catalytic

Table 4. Methyl Acetate (MeOAc) Hydrogenation over S-CNTs Based Catalysts and L-CNTs Based Catalysts

supports	catalysts	conversion (%) MeOAc	selectivity (mol, %) MeOH	EtOH	EtOAc	TOF[a] (10^{-2} s^{-1})
S-CNTs	Cu-S	11.3	58.6	27.2	14.2	5.9
	Cu-S-673	17.3	57.8	25.5	16.7	6.8
	Cu-S-973	22.5	56.8	27.6	15.6	7.0
	Cu-S-1173	19.5	57.1	26.6	16.3	8.1
L-CNTs	Cu-L	13.9	55.3	31.9	12.8	6.5
	Cu-L-673	4.6	56.4	37.1	6.5	3.9
	Cu-L-973	4.5	55.8	38.3	5.9	4.0
	Cu-L-1173	4.1	56.0	38.2	5.8	3.7

[a]TOF is the MeOAc turnover frequency, which defined as the number of converted MeOAc molecules in 100 s over one active site. The number of active sites (Cu atoms exposed on the surface of particles) is determined by N_2O pulse method. Reaction conditions: temperature = 493 K; pressure = 3 MPa; catalyst weight = 0.5 g; reaction time = 2 h; F (H_2) = 80 mL/min; F (MeOAc) = 0.9 g/h; MeOAc = methyl acetate; EtOAc = ethyl acetate; MeOH = methanol; EtOH = ethanol.

activity than that of unannealed Cu-L. The highest activity catalyst was Cu-L with the conversion of 13.9% and the molar selectivity to ethanol of 31.9%. Compared with Cu-S catalyst, both the conversion and the selectivity of ethanol were higher for Cu-L. The higher activity of Cu-L catalyst might come from the follow reasons: First, the starting reduction temperature of Cu-L (Figure 9) was lower than that of the Cu-S (Figure 6), which guaranteed that the highly dispersed Cu_xO in Cu-L was easier to be reduced. Second, the catalyst with larger metallic Cu surface area usually has higher conversion in this hydrogenation reaction.[55] Third, the higher selectivity to ethanol of catalyst Cu-L was considered to be derived from the larger tube diameter based catalyst, which was relatively inert to trans-esterification.[9] The conversion of MeOAc decreased after heat treatment for L-CNTs catalysts, which was different from the changing trend of S-CNTs based catalysts. TPR patterns disclosed that the amount of bulk Cu_xO in L-CNTs based catalysts increased dramatically with the enhancement of heat treatment temperature, which was not a benefit to the catalysis of the reaction of MeOAc to ethanol. However, the bulk Cu_xO amount inside the S-CNTs based catalysts only gradually increased because of the space confinement effect of S-CNTs. Above all, the high ratio of highly dispersion Cu and the low reduction temperature helps to improve the Cu exposed area, which, in turn, enhances the catalytic performance.

3.6. MeOAc Hydrogenation on Cu Nanoparticles Loaded Outside CNTs Catalysts. The catalyst with the same amount of Cu nanoparticles loaded outside CNTs was prepared and analyzed to highlight the confinement effect of CNTs. Figure 10a shows the TEM image of C-S-CNTs. Different to S-CNTs (Figure 1b), C-S-CNTs treated by diluted nitric acid (37.5%) presented most ends still unopened. The TEM image of Cu-C-S is displayed in Figure 10b. Most Cu nanoparticles were deposited evenly on the outer surface of CNTs. The formation of Cu nanoparticles decorated outside

dx.doi.org/10.1021/cs300234e | ACS Catal. 2012, 2, 1958−1966

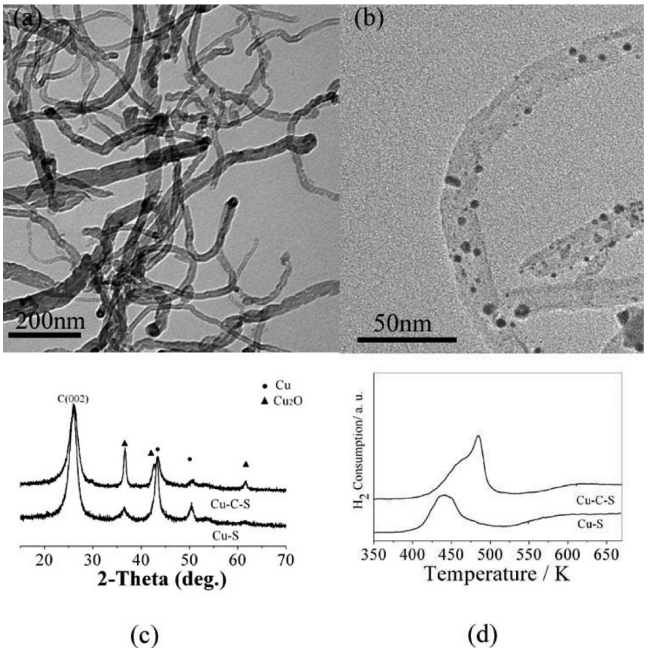

Figure 10. TEM images of (a) C-S-CNTs, (b) Cu-C-S, (c) XRD patterns of Cu-S and Cu-C-S, (d) TPR patterns of Cu-S and Cu-C-S.

CNTs is due to the closed ends that prevent Cu nanoparticles to enter the channel of C-S-CNTs. The XRD patterns of Cu-S and Cu-C-S catalysts after calcination in Ar atmosphere are compared in Figure 10c. As discussed above, autoreduction happened on the Cu nanoparticles in CNTs during the process of oxygen-free calcination. More metallic Cu was detected on Cu-S than Cu-C-S catalysts, indicating that the Cu nanoparticles loaded inside CNTs channels is easier to be autoreduced than those outside of CNTs. MeOAc hydrogenation catalyzed by Cu nanoparticles loaded inside or outside CNTs catalyst is compared in Table 5. It is noteworthy that the

Table 5. MeOAc Hydrogenation over Cu-S and Cu-C-S Catalysts[a]

	conversion (%)	selectivity (mol, %)		
catalysts	MeOAc	MeOH	EtOH	EtOAc
Cu-S	11.3	58.6	27.2	14.2
Cu-C-S	7.4	55.9	32.6	11.5

[a]Reaction conditions: temperature = 493 K; pressure = 3 MPa; catalyst weight = 0.5 g; reaction time = 2 h; F (H_2) = 80 mL/min; F (MeOAc) = 0.9 g/h; MeOAc = methyl acetate; EtOAc = ethyl acetate; MeOH = methanol; EtOH = ethanol.

conversion obtained on Cu-S catalyst was 11.3%, obviously higher than 7.4% of Cu-C-S catalyst. The higher catalytic activity of Cu-S catalyst should be attributed to the following three reasons: First, the reducibility of the supported Cu species is a crucial factor to its catalytic performance. The H_2 TPR profiles of the Cu-S and Cu-C-S catalysts are compared in Figure 10d. It was evident that the reduction peaks of two catalysts were well consistent with their catalytic activities, indicating that the more difficult the reduction of the catalyst, the less catalytic activity it has. Second, it has been reported that some gases such as CO and H_2 molecules can be enriched inside the CNTs channels. The increased H_2 concentration inside CNTs channels can accelerate the reaction rate and finally improve the catalytic performance. The third reason is the space confinement effect of the CNTs which can effectively prevent the growth of nanoparticles inside of CNTs channels and simultaneously suppress the deactivation of catalyst. The size changes on Cu nanoparticles in Cu-S and Cu-C-S after MeOAc hydrogenation reaction are shown in Figure 11. It was obvious that the size of Cu nanoparticles in Cu-S increased less than that in Cu-C-S because of the space confinement effect.

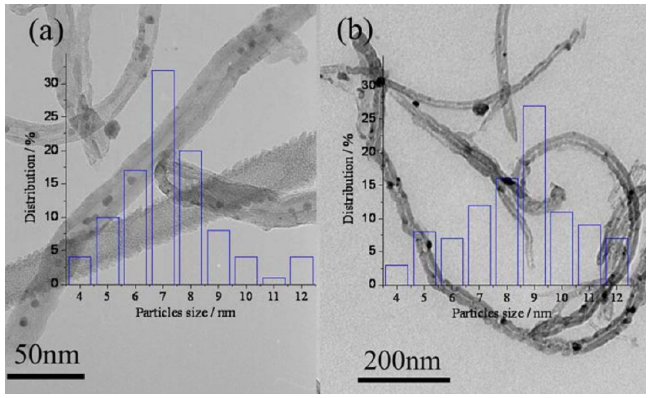

Figure 11. TEM photos of catalysts after reaction. (a) Cu-S, (b) Cu-C-S.

4. CONCLUSION

The hydrogenation catalysts, Cu nanoparticles filled CNTs, were prepared via a convenient wet chemical approach. MeOAc hydrogenation was selected as the probe reaction to study the catalytic performance and the confinement effects of Cu nanoparticles filled CNTs. The results showed that CNTs with smaller inner diameter unprecedentedly exhibited stronger autoreduction effect on Cu nanoparticles confined inside its channels. The heat treatment, a critical parameter, was also proven, which brought beneficial effect on the catalytic performance of small inner diameter CNTs derivative with an optimum temperature of 973 K. However, negative effect of annealing was found for L-CNTs based catalyst. Furthermore, the Cu filled inside CNTs catalyst showed higher catalytic performance than the Cu nanoparticles loaded outside CNTs catalyst. It is believed that the synergistic effects created by CNTs tube diameter, the location of loaded catalyst, as well as heat treatment, result in different confinement effect and catalytic performance when metal loaded CNTs are used as catalyst. This work will provide a new perspective to design and synthesize related catalysts with excellent performance.

AUTHOR INFORMATION

Corresponding Author

*E-mail: tsubaki@eng.u-toyama.ac.jp (N.T.), wmbpeter@yahoo.com.cn (M.W.).

Notes

The authors declare no competing financial interest.

REFERENCES

(1) Iijima, S. *Nature* **1991**, *354* (6348), 56−58.
(2) Serp, P.; Castillejos, E. *ChemCatChem* **2010**, *2* (1), 41−47.
(3) Pan, X. L.; Bao, X. H. *Chem. Commun.* **2008**, *47*, 6271−6281.
(4) Ovejero, G.; Sotelo, J. L.; Rodriguez, A.; Diaz, C.; Sanz, R.; Garcia, J. *Ind. Eng. Chem. Res.* **2007**, *46* (20), 6449−6455.

(5) Kang, J. C.; Zhang, S. L.; Zhang, Q. H.; Wang, Y. *Angew. Chem., Int. Ed.* **2009**, *48*, 2565−2568.
(6) Zarubova, S.; Rane, S.; Yang, J.; Yu, Y. D.; Zhu, Y.; Chen, D.; Holmen, A. *ChemSusChem* **2011**, *4* (7), 935−942.
(7) Tavasoli, A.; Abbaslou, R. M. M.; Trepanier, M.; Dalai, A. K. *Appl. Catal., A* **2008**, *345* (2), 134−142.
(8) Pan, X. L.; Bao, X. H. *Acc. Chem. Res.* **2011**, *44* (8), 553−562.
(9) Santiso, E. E.; George, A. M.; Turner, C. H.; Kostov, M. K.; Gubbins, K. E.; Buongiorno-Nardelli, M.; Sliwinska-Bartkowiak, M. *Appl. Surf. Sci.* **2005**, *252* (3), 766−777.
(10) Chen, W.; Pan, X. L.; Bao, X. H. *J. Am. Chem. Soc.* **2007**, *129*, 7421−7426.
(11) Tavasoli, A.; Trepanier, M.; Dalai, A. K.; Abatzoglou, N. *J. Chem. Eng. Data* **2010**, *55* (8), 2757−2763.
(12) Yang, H. X.; Song, S. Q.; Rao, R. C.; Wang, X. Z.; Yu, Q.; Zhang, A. M. *J. Mol. Catal. A: Chem.* **2010**, *323* (1−2), 33−39.
(13) Pan, X. L.; Fan, Z. L.; Chen, W.; Ding, Y. J.; Luo, H. Y.; Bao, X. H. *Nat. Mater.* **2007**, *6* (7), 507−511.
(14) Zhang, H.; Lancelot, C.; Chu, W.; Hong, J. P.; Khodakov, A. Y.; Chernavskii, P. A.; Zheng, J.; Tong, D. G. *J. Mater. Chem.* **2009**, *19*, 9241−9249.
(15) Zhu, Y. Y.; Wang, S. R.; Zhu, L. J.; Ge, X. L.; Li, X. B.; Luo, Z. Y. *Catal. Lett.* **2010**, *135* (3−4), 275−281.
(16) Yang, R. Q.; Yu, X. C.; Zhang, Y.; Li, W. Z.; Tsubaki, N. *Fuel* **2008**, *87* (4−5), 443−450.
(17) Knapp, R.; Wyrzgol, S. A.; Jentys, A.; Lercher, J. A. *J. Catal.* **2010**, *276* (2), 280−291.
(18) Kim, J. Y.; Park, J. C.; Kang, H.; Song, H.; Park, K. H. *Chem. Commun.* **2010**, *46*, 439−441.
(19) Zhang, Z. F.; Dong, C. M.; Yang, C. H.; Hu, D.; Long, J.; Wang, L.; Li, H.; Chen, Y.; Kong, D. L. *Adv. Synth. Catal.* **2010**, *352*, 1600−1604.
(20) Alonso, F.; Moglie, Y.; Radivoy, G.; Yus, M. *Eur. J. Org. Chem.* **2010**, 1875−1884.
(21) Evano, G .; Blanchard, N.; Toumi, M. *Chem. Rev.* **2008**, *108*, 3054−3131.
(22) Ranu, B. C.; Dey, R.; Chatterjee, T.; Ahammed, S. *ChemSusChem* **2012**, *5*, 22−44.
(23) Wang, Z. Y.; Zhao, Z. B.; Qiu, J. S. *Carbon* **2006**, *44* (9), 1845−1847.
(24) Zhang, G. Y.; Wang, E. G. *Appl. Phys. Lett.* **2003**, *82* (12), 1926−1928.
(25) Ye, X. R.; Lin, Y. H.; Wang, C. M.; Wai, C. M. *Adv. Mater.* **2003**, *15* (4), 316−319.
(26) Wang, X. Y.; Zhang, F.; Xia, B. Y.; Zhu, X. F.; Chen, J. S.; Qiu, S. L.; Zhang, P.; Li, J. X. *Solid State Sci.* **2009**, *11* (3), 655−659.
(27) Yu, Y.; Ma, L. L.; Huang, W. Y.; Du, F. P.; Yu, J. C.; Yu, J. G.; Wang, J. B.; Wong, P. K. *Carbon* **2005**, *43* (3), 670−673.
(28) Wang, P.; Huang, B. B.; Wei, J. Y.; Qin, X. Y.; Yao, S. S.; Zhang, Q. *Mater. Lett.* **2007**, *61* (30), 5255−5257.
(29) Li, X. G.; San, X. G.; Zhang, Y.; Ichii, T.; Meng, M.; Tan, Y. S.; Tsubaki, N. *ChemSusChem* **2010**, *3* (10), 1192−1199.
(30) Hsin, Y. L.; Hwang, K. C.; Yeh, C. T. *J. Am. Chem. Soc.* **2007**, *129* (32), 9999−10010.
(31) Raymundo-Piñero, E.; Cacciaguerra, T.; Simon, P.; Béguin, F. *Chem. Phys. Lett.* **2005**, *412*, 184−189.
(32) Zhou, J. S.; Song, H. H.; Fu, B. C.; Wu, B.; Chen, X. H. *J. Mater. Chem.* **2010**, *20* (14), 2794−2800.
(33) Maldonado, S.; Morin, S.; Stevenson, K. J. *Carbon* **2006**, *44* (8), 1429−1437.
(34) Lin, K. Y.; Chang, J. K.; Chen, C. Y.; Tsai, W. T. *Diamond Relat. Mater.* **2009**, *18* (2−3), 553−556.
(35) Scheibe, B.; Borowiak-Palen, E.; Kalenczuk, R. J. *Mater. Charact.* **2010**, *61* (2), 185−191.
(36) Bystrzejewski, M.; Huczko, A.; Lange, H.; Gemming, T.; Büchner, B.; Rümmeli, M. H. *J. Colloid Interface Sci.* **2010**, *345*, 138−142.
(37) Wang, L.; Ge, L.; Rufford, T. E.; Chen, J.; Zhou, W.; Zhu, Z. H.; Rudolph, V. *Carbon* **2011**, *49* (6), 2022−2032.
(38) Kim, D. Y.; Yang, C. M.; Park, Y. S.; Kim, K. K.; Jeong, S. Y.; Han, J. H.; Lee, Y. H. *Chem. Phys. Lett.* **2005**, *413* (1−3), 135−141.
(39) Sun, Y. F.; Zhang, A. M.; Yin, Y.; Dong, Y. M.; Cui, Y. C.; Zhang, X.; Hong, J. M. *Mater. Chem. Phys.* **2007**, *101* (1), 30−34.
(40) Yang, Q. H.; Hou, P. X.; Bai, S.; Wang, M. Z.; Cheng, H. M., C. *Chem. Phys. Lett.* **2001**, *345* (1−2), 18−24.
(41) Serp, P.; Corrias, M.; Kalck, P. *Appl. Catal., A* **2003**, *253* (2), 337−358.
(42) Hou, Y.; Cheng, Y. W.; Hobson, T.; Liu, J. *Nano Lett.* **2010**, *10* (7), 2727−2733.
(43) Chen, H.; Yang, S.; Yu, K.; Ju, Y.; Sun, C. *J. Phys. Chem. A* **2011**, *115* (14), 3034−3041.
(44) Chen, W.; Pan, X. L.; Willinger, M. G.; Su, D. S.; Bao, X. H. *J. Am. Chem. Soc.* **2006**, *128* (10), 3136−3137.
(45) Xiong, H.; Moyo, M.; Rayner, M. K.; Jewell, L. L.; Billing, D. G.; Coville, N. J. *ChemCatChem* **2010**, *2* (5), 514−518.
(46) Xiong, H.; Motchelaho, M. A. M.; Moyo, M.; Jewell, L. L.; Coville, N. J. *J. Catal.* **2011**, *278*, 26−40.
(47) Pawelec, B.; La Parola, V.; Navarro, R. M.; Murcia-Mascaros, S.; Fierro, J. L. G. *Carbon* **2006**, *44* (1), 84−98.
(48) Eswaramoorthi, I.; Sundaramurthy, V.; Dalai, A. K. *Appl. Catal., A* **2006**, *313* (1), 22−34.
(49) Soares, O.; Orfao, J. J. M.; Pereira, M. F. R. *Ind. Eng. Chem. Res.* **2010**, *49* (16), 7183−7192.
(50) Dow, W. P.; Wang, Y. P.; Huang, T. J. *Appl. Catal., A* **2000**, *190* (1−2), 25−34.
(51) Yin, A. Y.; Guo, X. Y.; Fan, K. N.; Dai, W. L. *ChemCatChem* **2010**, *2* (2), 206−213.
(52) Zhu, Z. H.; Zhu, H. Y.; Wang, S. B.; Lu, G. Q. *Catal. Lett.* **2003**, *91* (1−2), 73−81.
(53) Dong, X.; Zhang, H. B.; Lin, G. D.; Yuan, Y. Z.; Tsai, K. R. *Catal. Lett.* **2003**, *85* (3−4), 237−246.
(54) Cheung, P.; Bhan, A.; Sunley, G. J.; Iglesia, E. *Angew. Chem., Int. Ed.* **2006**, *45*, 1617−1620.
(55) Balaraju, M.; Rekha, V.; Prasad, P. S. S.; Prasad, R. B. N.; Lingaiah, N. *Catal. Lett.* **2008**, *126* (1−2), 119−124.